Regional Studies in Marine Science 18 (2018) 1–10

Contents lists available at ScienceDirect

Regional Studies in Marine Science

journal homepage: www.elsevier.com/locate/rsma

Seasonal variations of hydrographic parameters off the Sudanese coast of the Red Sea, 2009–2015

Elsheikh B. Ali [a,b,*], James H. Churchill [c], Knut Barthel [a], Ingunn Skjelvan [d,a], Abdirahman M. Omar [d,a], Tor E. de Lange [a], Elfatih B.A. Eltaib [b]

[a] Geophysical Institute (GFI), University of Bergen (UiB), Bergen, Norway
[b] Institute of Marine Research (IMR), Red Sea University (RSU), Port Sudan, Sudan
[c] Department of Physical Oceanography, Woods Hole Oceanographic Institution, Woods Hole, MA 02543, USA
[d] Uni Research Climate, Bergen, Norway

HIGHLIGHTS

- Prominent seasonal temperature and salinity cycles observed in western Red Sea.
- The seasonal salinity signal lags that of temperature by roughly 3 months.
- The seasonality is partly due to local heat/mass flux through the sea surface.
- Alongshore advection is also important for the seasonality pattern of temperature and salinity.

ARTICLE INFO

Article history:
Received 11 May 2017
Received in revised form 12 December 2017
Accepted 12 December 2017
Available online 21 December 2017

Keywords:
Coastal Red Sea
Temperature
Salinity
Time series
Seasonality
Alongshore advection

ABSTRACT

The variations of temperature and salinity in the Sudanese coastal zone of the Red Sea are studied for the first time using measurements acquired from survey cruises during 2009–2013 and from a mooring during 2014–2015. The measurements show that temperature and salinity variability above the permanent pycnocline is dominated by seasonal signals, similar in character to seasonal temperature and salinity oscillations observed further north on the eastern side of the Red Sea. Using estimates of heat flux, circulation and horizontal temperature/salinity gradients derived from a number of sources, we determined that the observed seasonal signals of temperature and salinity are not the product of local heat and mass flux alone, but are also due to alongshore advection of waters with spatially varying temperature and salinity. As the temperature and salinity gradients, characterized by warmer and less saline water to the south, exhibit little seasonal variation, the seasonal salinity and temperature variations are closely linked to an observed seasonal oscillation in the along-shore flow, which also has a mean northward component. We find that the inclusion of the advection terms in the heat and mass balance has two principal effects on the computed temperature and salinity series. One is that the steady influx of warmer and less saline water from the south counteracts the long-term trend of declining temperatures and rising salinities computed with only the local surface flux terms, and produces a long-term steady state in temperature and salinity. The second effect is produced by the seasonal alongshore velocity oscillation and most profoundly affects the computed salinity, which shows no seasonal signal without the inclusion of the advective term. In both the observations and computed results, the seasonal salinity signal lags that of temperature by roughly 3 months.

1. Introduction

Encompassing a highly diverse ecosystem, the Red Sea ranks as one of the warmest and most saline of the world's seas (Belkin, 2009; Raitsos et al., 2011). Fluctuations in near-surface temperature and salinity within Red Sea coastal waters can have profound ecological consequences, particularly for the numerous reef systems that fringe the Red Sea basin (Cantin et al., 2010). It is well established that the growth rate and overall health of coral communities are highly sensitive to changes in temperature and affected to a lesser degree by variations in salinity (e.g., Ferrier-Pages et al., 1999; Furby et al., 2013; Kuanui et al., 2015).

* Corresponding author at: Institute of Marine Research (IMR), Red Sea University (RSU), Port Sudan, Sudan.
E-mail addresses: elsheikh.ali@gfi.uib.no, sheikhbashirali@yahoo.com (E.B. Ali).

https://doi.org/10.1016/j.rsma.2017.12.004

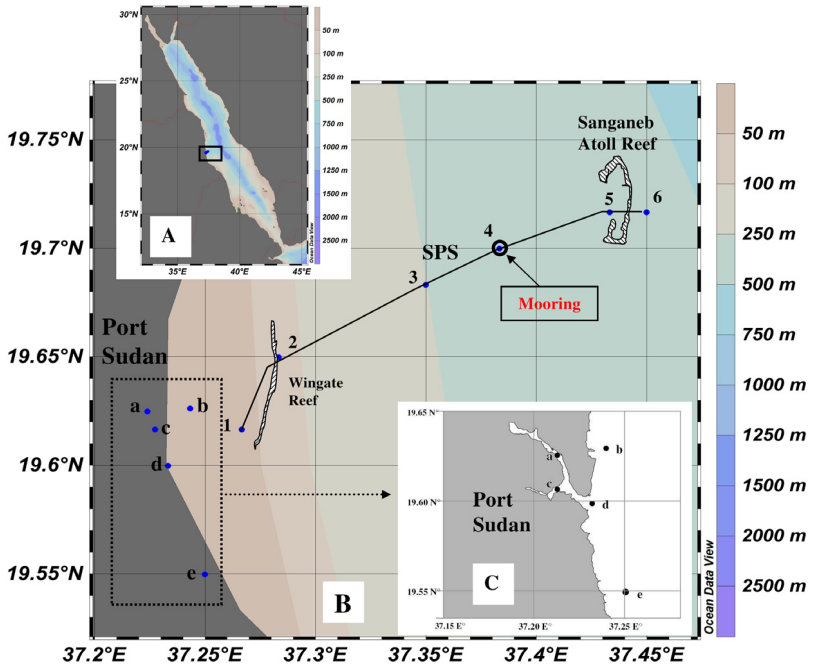

Fig. 1. (A) The Red Sea with our study area enclosed in the black-bordered box. (B) Locations of our observations: the Sanganeb section (SPS; black solid line connecting six CTD stations) and Port Sudan Harbor stations (PSH; five CTD stations labeled a–e), and a CTD mooring (at the same position of station 4 in SPS). (C) PSH stations in detail: (a) IMR jetty, (b) Abu Hashish lagoon, (c) Khor Kilab, (d) Harbor Inlet, and (e) Refinery stations.

Further, it is shown that temperature is also linked to the growth of phytoplankton in the Red Sea, as the monsoon-driven horizontal advection of colder and nutrient rich waters into the Red Sea from the Gulf of Aden promotes phytoplankton blooms and maintains the productivity in large parts of the Red Sea during winter (Raitsos et al., 2015) and summer (Dreano et al., 2016; Wafar et al., 2016). It is also well established that changes in temperature and salinity affect the inorganic carbon cycle; e.g. warmer water reduces the gas solubility and thus increases the flux of carbon dioxide from the surface water into the atmosphere, and changes in alkalinity are tightly connected to changes in salinity (e.g. Sarmiento and Gruber, 2006).

There are currently few published studies of the temporal variations of temperature or salinity within the Red Sea. Churchill et al. (2014a) examined temperature fluctuations waters of the coastal zone of the central Red Sea off the Saudi Arabian coast using data acquired from moorings deployed at ∼50 m depth. They showed that near-surface (upper 15 m) temperature variations span a range of order 8 °C and are predominately due to a seasonal signal with a range of order 6 °C. A seasonal near-surface temperature signal with a similar range was reported by Sultan and Ahmad (1991) based on sea surface measurements acquired off of Jeddah Saudi Arabia, by Berman et al. (2003) based on hydrographic data acquired in summer and winter, and by Davis et al. (2011) based on temperature sensors placed on platform reef tops. Published reports of temporal salinity variations in the Red Sea are very rare. Churchill et al. (2014a) briefly discussed salinity records from the moorings referenced above but showed no time series. Sultan and Ahmad (1991) presented an 8-year record of monthly-averaged surface salinities acquired off of Jeddah Saudi Arabia that span a range of the order of 1 psu, but noted that the salinities may have been affected by discharge from the Jeddah desalinization facility.

It is notable that all of the studies reviewed above utilized data from the coastal zone of the central Red Sea west of the Saudi Arabian coast and so may not be representative of temperature and salinity variations over the full Red Sea. Furthermore, no study has dealt fully with the dynamics responsible for the observed temperature and salinity variations. While some studies have related temperature variations to surface heat flux (Sultan and Ahmad, 1991; Berman et al., 2003; Churchill et al., 2014a), the manner in which temperature and salinity variations are influenced by water mass transport has not yet been assessed.

It may be expected that near-surface temperature and salinity may undergo seasonal changes related to the impact of monsoon winds on the circulation of the Red Sea. During winter, strong south-southeasterly winds prevail over the southern Red Sea and drive a surface inflow of relatively cold and fresh water from the Gulf of Aden into the Red Sea (Patzert, 1974). During summer, north-northwesterly winds tend to extend over much of the Red Sea (Sofianos and Johns, 2001), and may drive more saline surface water in the northern Red Sea to the south. Notably, monsoon winds are responsible for the subsurface influx of relatively cold and fresh Gulf of Aden Intermediate Water (GAIW), which enters the Red Sea through the Bab-al-Mandab Strait during the summer as a result of wind-induced upwelling in the Gulf of Aden (Morcos, 1970; Pedgley, 1974; Patzert, 1974; Morcos and Soliman, 1974; Quadfasel and Bauner, 1993; Aiki et al., 2006; Churchill et al., 2014b; Yao et al., 2014a, b; Zhai et al., 2015).

The work reported here is aimed at furthering the understanding of temperature and salinity variations in the coastal Red Sea. Using data from moored instruments and hydrographic surveys, we describe the temporal variations in temperature and salinity within near-surface coastal waters off of Port Sudan, Sudan (Fig. 1). With the aid of reanalysis and satellite-derived data, we examine the mechanisms responsible for these variations, concentrating on the relative importance of local processes (surface heat and mass flux) and water mass advection. Our focus is on the seasonal signals of temperature and salinity. As noted above, previous observations have shown that the range of near-surface temperature variation in the central Red Sea is primarily due to the seasonal signal.

In the following sections, we first describe the data sets and methodology employed (Section 2). We then detail the temperature and salinity variations in the coastal zone off of Port Sudan (Section 3.1) and examine the dominant mechanisms responsible for these variations (Section 3.2). We conclude with a summary of our findings and a discussion of how they relate to prior work on the dynamics of the Red Sea system (Section 4).

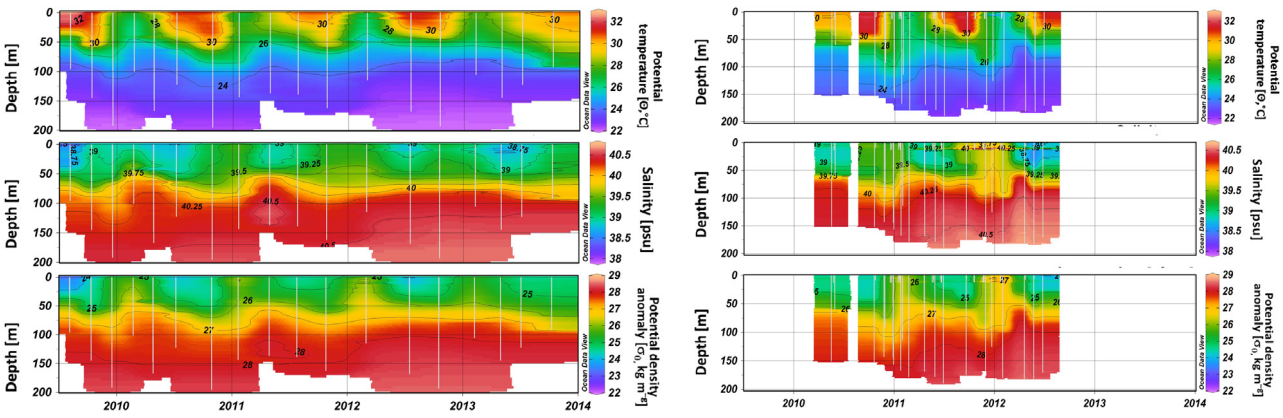

Fig. 2. Depth/time contours of physical parameters. The left panels are averages values from the Sanganeb—Port Sudan section (SPS; Station 1–6) and the right panels are averages values from Port Sudan harbor stations (PSH; IMR jetty, Abu Hashish lagoon, Khor Kilab, Harbor Inlet, and Refinery stations). The vertical white lines indicate the measurements times and depth.

Table 1
Data sources.

Name of dataset	Period	Sampling/frequency	Stations/resolution	Parameters/Depth
1. Cruises data				
a. Sanganeb—Port Sudan Section (SPS)	2009–2013	3–4 times/year	6	T, S, P/surface to ∼200 m
b. Port Sudan Harbor (PSH)	2010–2012	2–9 times/year	5	T, S, P/surface to ∼150 m
2. Mooring data	01/10/2014–15/10/2015	Hourly	At station 4 of SPS	T, S/37 m
3. Satellite-derived SST from NOAA	2009–2014	Daily	Position near station 4 of SPS/0.25° × 0.25°	SST/surface
4. Simple Ocean Data Assimilation (SODA)	2009–2010	Monthly	0.25° × 0.4°	Horizontal T and S gradients/ average over upper 50 m
5. NCEP data Reanalysis-2	2009–2014	6 hourly	Cell centered at 37.50° E, 20.00° N/2° × 2°	Surface wind speed, heat flux, and mass flux/surface
6. Sea Level Anomaly (SLA)-AVISO	2009–2014	Daily	0.25° × 0.25°	Geostrophic current field computed from SLA/surface

2. Data and methods

Our analysis employed six datasets (Table 1). Three were used to describe the seasonal variation of temperature, salinity and potential density (σ_θ) off of Port Sudan, and three were employed in assessing the mechanisms responsible for the seasonal variation of these properties. Below, we detail these data sets and present our methods for estimating near-surface temperature and salinity change.

2.1. Measurements of coastal temperature and salinity

2.1.1. Cruises data (2009–2013)

Our study employed cruise measurements of temperature and salinity acquired at two sets of stations (Fig. 1): near-shore stations in the area of Port Sudan Harbor (PSH), and stations situated along a section between the Sanganeb atoll reef (30 km northeast of Port Sudan) and Port Sudan (Sanganeb—Port Sudan section, SPS). The data acquired at all stations were from a SAIV A/S model 204 CTD, deployed using a hand winch and equipped with an inductive cell conductivity sensor (resolution 0.01 ms cm^{-1}, accuracy ±0.02 ms cm^{-1}), a temperature sensor (resolution 0.001, accuracy ±0.01 °C), and a pressure sensor (resolution 0.01 mbar, accuracy ±0.02%). The SPS and PSH surveys were organized by IMR–RSU in Port Sudan and conducted on one of the Sudanese Marine Security Department ships.

The salinity was computed to a resolution of 0.01 psu and to an accuracy of ±0.02 psu (SAIV, 2006). Calibration of the salinity measurements was done using water samples acquired during a subset of the CTD casts by a Hydrobios (2 l) water sampler. The bottle salinity was determined using the Guildline Portasal Salinometer (model 8410A) to an accuracy of ±0.003 psu (Guildline, 2002). The CTD salinities were calibrated using measurements from the Salinometer, and adjustments were applied to salinities from each of the SPS and PSH cruises.

Measurements at the PSH stations encompassed the period of 2010–2012 and extended vertically from near the surface to roughly 150 m depth. Measurements from the SPS transect were from 2009–2013 and vertically extended to roughly 200 m. Both sets of data resolved the seasonal signal of temperature and salinity (Fig. 2). The SPS data were taken at a quarterly interval (collected roughly during October, February, April, and July), whereas the PSH data interval was shorter but varied considerably.

2.1.2. Mooring data (2014–2015)

Additional temperature and salinity time series data of our study were acquired from a Sea Bird CTD (SBE 37-SM MICROCAT, SN 3939) affixed to a mooring deployed on 1 October 2014 at station 4 (37.395°E, 19.720°N; Fig. 1) of SPS transect. The bottom depth at the mooring location was ∼800 m, and the CTD, which was positioned at a nominal depth of 37 m, was set to record at hourly intervals. The mooring was recovered on 15 October 2015. The CTD was equipped with conductivity (resolution 0.0001, accuracy ±0.003 ms cm^{-1}), temperature (resolution 0.0001, accuracy ±0.002 °C), and pressure (resolution 0.002%, accuracy ±0.1%) sensors. The CTD salinity were calibrated as described above, using bottle salinity samples collected immediately after deployment of the mooring.

2.1.3. Satellite-derived sea surface temperature (2009–2014)

The sea surface temperature (SST) data used in this study were from the NOAA High-resolution Blended Analysis of Daily SST (Version 2) dataset (Reynolds et al., 2007). Formulated by combining observations from different platforms (satellites, ships, buoys),

the dataset is comprised of daily temperatures specified on a 0. 25° latitude by 0. 25° longitude global grid. Similar SST data (with 0.25° × 0.25° resolution) have recently been employed by Dreano et al. (2016) in a study of the effect of GAIW on phytoplankton blooms in the southern Red Sea.

2.2. Data used to compute heat and salt fluxes

2.2.1. The Simple Ocean Data Assimilation (SODA) dataset (2009)

The SODA dataset is comprised of data produced by an ocean general circulation model with an average resolution of 0. 25° latitude by 0. 4° longitude, and 40 vertical levels. Direct contemporaneous observations are continuously used to correct the model error of the generated ocean variables (Carton and Giese, 2008). SODA data have been employed by Manasrah et al. (2009) in a study of sea level variations over the Red Sea. We employed SODA data to estimate horizontal salinity and temperature gradients, which were used in the computation of heat and salt fluxes due to horizontal advection.

2.2.2. NCEP datasets (2009–2014)

We extracted data from the National Centers for Environmental Prediction (NCEP) / National Center for Atmospheric Research (NCAR) dataset to estimate the surface wind stress as well as surface heat and mass flux in our study region (Kalnay et al., 1996). All data were from a 2° latitude by 2° longitude cell centered at 37.50°E, 20.00°N. The wind stress was computed from 10 m NCEP Reanalysis-2 wind velocities according to the formulae of Large and Pond (1981).

To compute the surface heat flux, we downloaded individual surface heat flux components: net shortwave radiation (Q_{sw}), net longwave radiation (Q_{lw}), latent heat flux (Q_l) and sensible heat flux (Q_s). Net surface heat flux (Q_{net}) was determined according to (Wallcraft et al., 2008):

$$Q_{net} = Q_{sw} - Q_{lw} + Q_l + Q_s. \tag{1}$$

Net surface mass flux (m s^{-1}) was computed as:

$$M = E - P \tag{2}$$

where E is the evaporation rate and P is the precipitation rate. P was computed from the NCEP Reanalysis-2 precipitation rate (P_R, kg m^{-2} s^{-1}) according to:

$$P = \frac{P_R}{\rho_0} \tag{3}$$

where ρ_0 is the fresh water density. E was computed from the latent heat flux according to (Sumner and Belaineh, 2005):

$$E = \frac{-Q_l}{\rho_0 \lambda} \tag{4}$$

where λ is latent heat of vaporization of water (2.3×10^6 J kg^{-1}).

To assess the NCEP heat flux estimates, we compared the net heat flux series determined using measurements from an air–sea interaction buoy maintained (as part of a collaboration between Woods Hole Oceanographic Institution [WHOI] and King Abdullah University of Science and Technology [KAUST]) in the central Red Sea (at 38° 30.1′E; 22° 9.6′N) over 2008–2010 (Farrar et al., 2009; Bower and Farrar, 2015) with a net heat flux time series determined from NCEP data for the cell which included the buoy location. The two data series were highly correlated ($R^2 = 0.89$, $p < 0.001$) and exhibited closely matched seasonal cycles, with net heat flux into the ocean over March through September and net heat loss over the rest of the year. The net heat transfer over the two years of the comparison (2009–2010) was negative for both series, but was slightly larger in magnitude for the buoy-derived series (-1.2×10^9 versus -0.9×10^9 J m^{-2}).

2.2.3. Sea Level Anomaly (SLA) (2009–2014)

Estimation of near-surface velocities was done using altimeter-derived sea level anomaly (SLA) fields computed with respect to the CLS01 (Centre de Localization des Satellites) long-term mean sea surface height. Downloaded from AVISO (http://www.aviso.oceanobs.com/), the SLA fields were determined by combining sea level data from all available satellites and objectively mapping SLA on a 0. 25° latitude by 0. 25° longitude grid. We computed geostrophic surface velocity from the gridded SLA field through:

$$u_G = -\frac{g}{f}\frac{\partial \delta}{\partial y};\ v_G = \frac{g}{f}\frac{\partial \delta}{\partial x} \tag{5}$$

where δ is SLA, u_G and v_G are the east and north components of geostrophic velocity, respectively, g is the gravitational acceleration and f is local Coriolis parameter.

2.3. Estimation of near-surface temperature and salinity changes

With the data described above, we sought to roughly assess the contributions of surface heat and mass fluxes and horizontal advection in driving the observed seasonal signal of near-surface temperature and salinity in our study region. We did not consider the effects of mixing or vertical advection as these were not well suited for study with the available data. Our focus was on temperature and salinity changes in the layer above the permanent pycnocline. For simplicity, we assumed that this layer extended to a constant depth, h. We also assumed that the advective changes in temperature and salinity were principally due to fluxes of heat and salt in the alongshore direction (roughly N–S in the area of Port Sudan). This assumption is justified by the dominance of alongshore vs. across-shore flow observed in low-frequency current records measured in the coastal Red Sea (Churchill et al., 2014a). With these assumptions, the changes in temperature (T) and salinity (S) averaged over the surface layer may be approximated as:

$$\frac{\partial T}{\partial t} = \frac{Q_{net}}{h\rho_s C_p} - V\frac{\partial T}{\partial y} \tag{6}$$

$$\frac{\partial S}{\partial t} = \frac{M}{h}S - V\frac{\partial S}{\partial y} \tag{7}$$

where C_p is the specific heat capacity of water (4.2×10^3 J kg^{-1}), y is the alongshore coordinate, ρ_s is the near-surface density and V is the vertically-averaged alongshore velocity in the layer above the permanent pycnocline.

Our approach was to determine the near-surface temperature and salinity signal from observed starting values of T_o and S_0, respectively. For simplicity, we took the horizontal temperature and salinity gradients as constants (determined from the SODA data as explained in Section 2.2). With these assumptions, the seasonal temperature and salinity signals were estimated from

$$T(t) = T_0 + \int_0^t \left[\frac{Q_{net}(\tau)}{h\rho_s C_p} - V(\tau)\frac{\partial T}{\partial y}\right] d\tau \tag{8}$$

$$S(t) = S_0 + \int_0^t \left[\frac{M(\tau)}{h}S(\tau) - V(\tau)\frac{\partial S}{\partial y}\right] d\tau. \tag{9}$$

3. Results

3.1. Seasonal variation

3.1.1. SPS and PSH

The measurements from the coastal hydrographic surveys (SPS and PSH) clearly show a seasonal signal in near-surface values of potential temperature (θ), salinity and potential density anomaly (σ_θ) (Fig. 2). The near-surface temperature signal is marked by maxima of close to 32 °C during summer and early autumn and

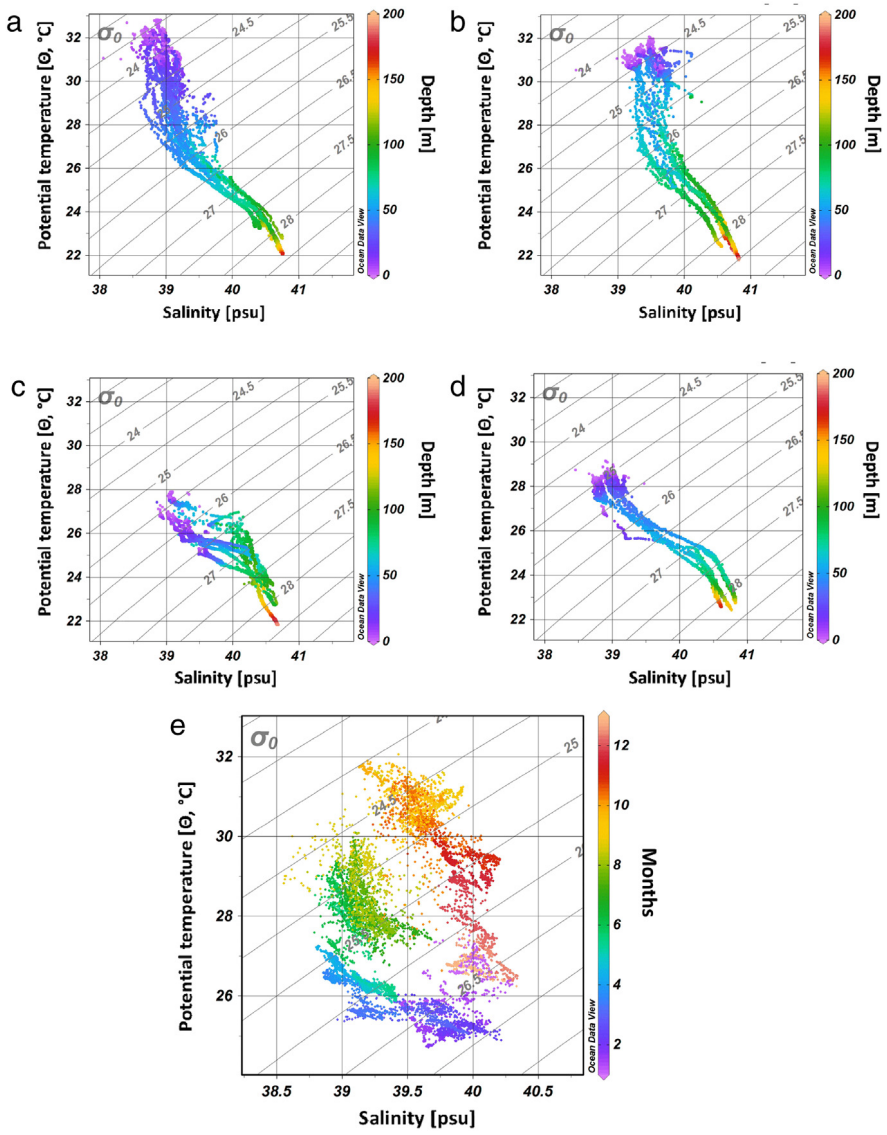

Fig. 3. Potential temperature–salinity (θ-S) diagrams during different seasons in the Red Sea (a) Summer, (b) autumn, (c) winter, and (d) spring. The colors indicate the depth of sampling, and data from the SPS section are used. (e) a θ-S diagram based on mooring data in which the colors indicate the month of sampling. The gray line contours refer to potential density anomaly [σ_θ, kg m^{-3}]. (For interpretation of the references to colour in this figure legend, the reader is referred to the web version of this article.)

minima of roughly 26 °C in winter. The timing and range of these maxima and minima closely match those of the seasonal temperature signals shown by Churchill et al. (2014a) based on moored measurements acquired in the coastal zone of the central Red Sea. In particular, Churchill et al. (2014a) show highest near-surface temperatures, of roughly 32 °C, over July–October contrasting with the lowest near-surface temperatures, of roughly 26 °C, over January–March (their Fig. 2). The seasonal near-surface salinity signal lags the temperature signal by roughly 3 months with maxima (39.0–39.5 psu at SPS and 39–40 psu at PSH) in late autumn/early winter and minima (approximately 38.5 psu in both areas) in late spring/early summer. The σ_θ seasonal signal is roughly the inverse of the temperature signal, with the densest water (σ_θ = 26–27 kg m^{-3}) appearing in winter whereas the lowest density water (24–25 kg m^{-3}) is seen in late summer/early autumn. The σ_θ data also reveal a seasonal variation in density vertical stratification over the upper 50 m characterized by nearly uniform σ_θ in winter and stronger stratification over the rest of the year. During all seasons, the top of the permanent pycnocline, roughly marked by the 26 σ_θ contour, appears at about 50 m depth (Fig. 2).

Potential temperature–salinity (θ-S) diagrams (Fig. 3a–d) clearly show a yearly progression in vertical stratification in the survey region. The σ_θ range over the vertical extent of the surveys is greatest during summer, extending from roughly 23.5 kg m^{-3} at the surface to 28.45 kg m^{-3} at 200 m. During summer, the density stratification in the upper 50 m, above σ_θ = 26 kg m^{-3}, is largely due to temperature stratification. The σ_θ range observed during autumn is slightly smaller, 23.9–28.5 kg m^{-3}. The higher near-surface densities of autumn relative to summer are principally due to the higher salinities observed in autumn. At σ_θ < 26 kg m^{-3}, salinities of the autumn surveys are roughly 0.5 psu greater than those of the summer surveys. The near-surface layer of strong temperature stratification seen in the summer and autumn surveys is absent during the winter surveys. The weak vertical temperature stratification observed in winter results in weak vertical density stratification, with σ_θ varying by about 0.5 kg m^{-3} in the upper 50 m. Near-surface vertical temperature and density gradients are slightly greater during the spring surveys, signaling the formation of the seasonal thermocline. It is noteworthy that during all seasons the largest temporal variations in θ, S and σ_θ occur above the permanent pycnocline (roughly at σ_θ < 26 kg m^{-3}), with

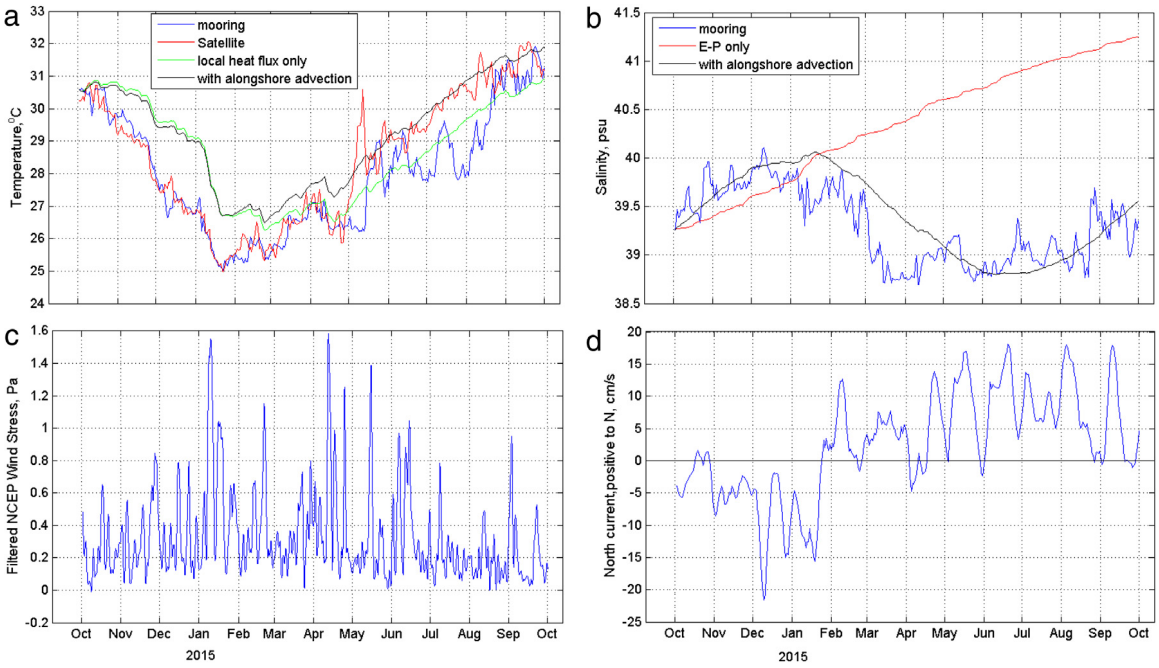

Fig. 4. (a) The seasonal variation of temperature (°C) from the mooring (blue line), from satellite (red line), computed from NCEP heat flux (green line), and computed with alongshore advection at station 4 close to the mooring (black line). (b) The seasonal variation of salinity (psu) from the mooring (blue line), computed from local evaporation/precipitation (red line), and computed with alongshore advection (black line). (c) The seasonal variation of the wind stress (Pa) calculated based on NCEP wind and filtered to 50-hour half-power period. (d) Velocity of northward geostrophic current (cm s^{-1}). (For interpretation of the references to colour in this figure legend, the reader is referred to the web version of this article.)

much smaller variations of these properties seen in the permanent pycnocline and below.

3.1.2. Mooring and SST data

The temperature and salinity records from the mooring (Fig. 4) show seasonal signals in close agreement with those exhibited by the cruise data. In particular, the mooring data show the order 3-month shift of the seasonal signal of salinity relative to temperature. The shift is particularly well defined by the temperature and salinity maxima, which occur, respectively, in late September 2015 and mid-December 2014. However, the shift is not as well defined by the minima of temperature and salinity. The seasonal decline in temperature occurs over the autumn and early winter and terminates in a clear minimum in mid-January 2015. By contrast, the seasonal salinity decline occurs over December 2014–March 2015 and is followed by a rise in salinity in August 2015. Both the salinity and temperature records show a dominant seasonal signal relative to higher frequency variations. The seasonal temperature signal extends over 6 °C, roughly from 25 to 31 °C, while the higher frequency variations are of magnitude 2 °C or less. The seasonal salinity signal is approximately 1.1 psu in magnitude, roughly from 38.7 to 39.8 psu, upon which fluctuations of order 0.4 psu are superimposed.

The distribution of θ-S derived from the mooring data (Fig. 3f) show a seasonal progression of near-surface density related to the seasonal variation of temperature and salinity. The increase in near-surface density from its minimum in October to its maximum in January is largely the product of declining temperatures, while the subsequent decline in near-surface density over January–April is principally due to a decrease in near-surface salinity. Completing the cycle, the May–October decrease in density is primarily the result of rising near-surface temperatures.

Comparing the moored temperature record with the satellite-derived SST record from the 0.25° latitude by 0.25° longitude cell encompassing the mooring indicates predominately well-mixed or weakly stratified conditions above the moored CTD (Fig. 4a). Significant temperature stratification above the mooring (indicated by a difference between the SST and mooring temperature) is confined to the period of early May through mid-August. However, the near-surface stratification is eroded on a number of occasions during this period (i.e. in mid-May, early June, and mid-July 2015). These mixing events appear to be at least partly due to the action of the surface wind stress and they correspond to peaks in the surface wind stress record derived from the NCEP winds (Fig. 4c).

The long-term (6-year) record of SST from the cell encompassing the mooring (Fig. 5a) very clearly shows the dominance of the seasonal signal over higher frequency variations. The seasonal SST signal spans a range of roughly 6 °C, between minima and maxima of 25 and 31 °C, whereas the magnitude of the higher frequency SST variations is at most 1 °C.

3.2. Factors controlling the seasonal signals

The observations reviewed above clearly show that the temporal variations of temperature and salinity above the permanent pycnocline in the near-shore region off of Port Sudan are dominated by seasonal signals that differ in phase by roughly 3 months (with the seasonal temperature signal leading). We now consider the extent to which these seasonal signals may be due to surface mass and heat flux (local processes) and to the effect of alongshore advection. We focus first on the impact of local processes on the seasonal signals.

3.2.1. Local processes

The change in mean temperature and salinity above the permanent pycnocline was estimated by evaluating Eqs. (8) and (9) with inclusion of only the first term in the integral of each equation. The depth of the layer above the permanent pycnocline, h , was approximated as 50 m based on the contoured temperature and salinity fields derived from survey data (Fig. 2).

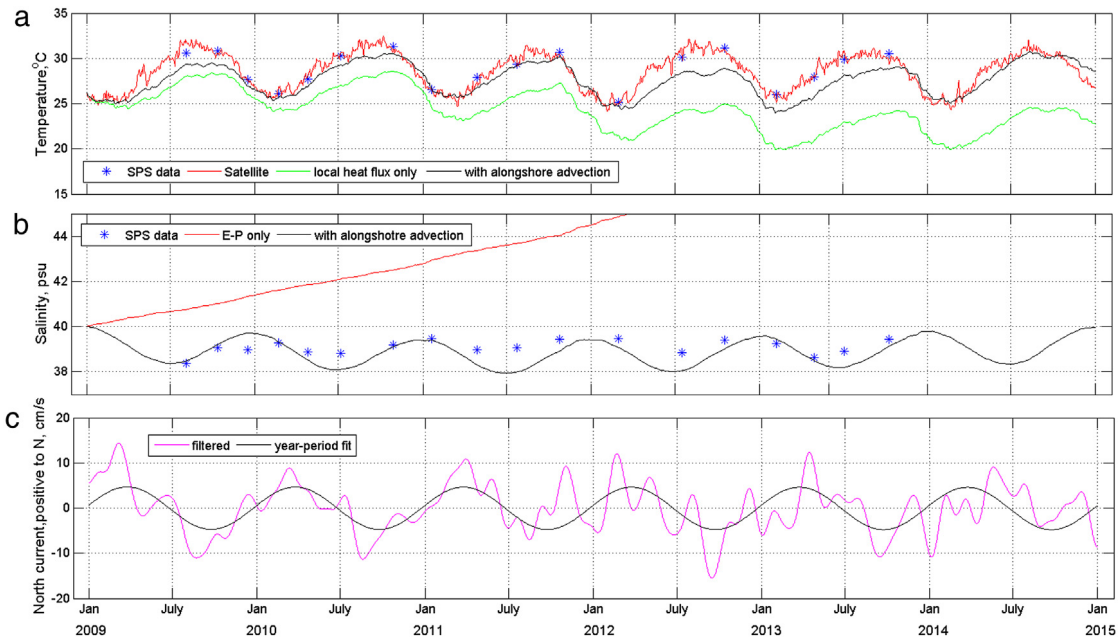

Fig. 5. The seasonality of near-surface temperature (a), salinity (b), and the northward geostrophic current (c). The different temperatures are; average temperature (over 50 m) from SPS data (blue stars), SST from satellite-derived data (red line), computed from NCEP heat flux (green line), and calculated with alongshore advection included (black line). The different salinities are; average salinity (over 50 m) from SPS transect (blue stars), calculated salinities based on local evaporation/precipitation (red line), and computed salinities with alongshore advection (black line) included. Shown in (c) are the northward geostrophic current off of Port Sudan, filtered with a 50-days half-power period filter (magenta line) and yearly-period velocity signal (black line). (For interpretation of the references to colour in this figure legend, the reader is referred to the web version of this article.)

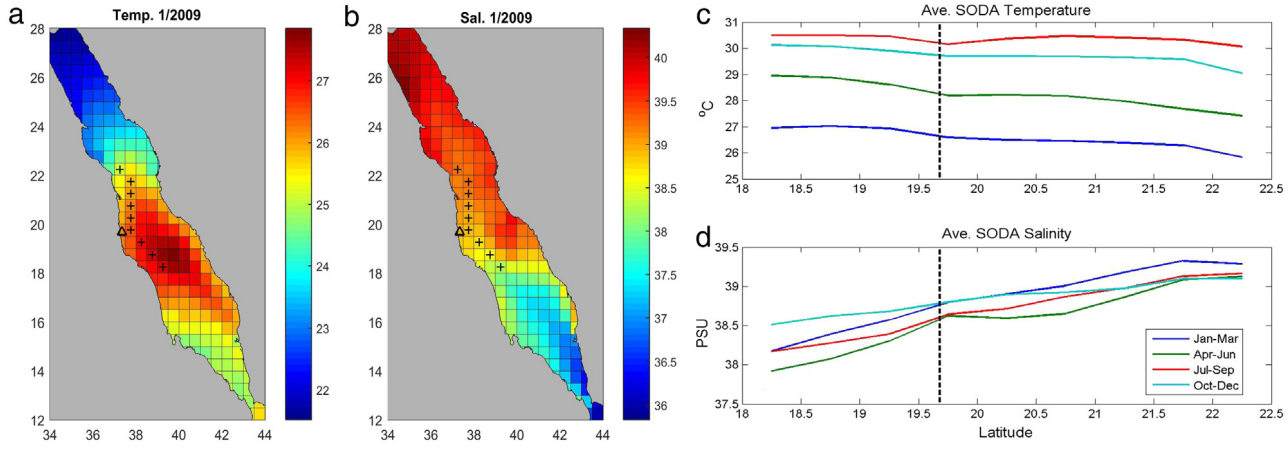

Fig. 6. Properties of mean temperature and salinity, averaged over the upper 50 m, as determined from SODA data. (a) Average temperature field of January 2009 with SODA grid cell indicated. (b) Average salinity field of January 2009. The open triangle in (a) and (b) marks the location of our study's mooring. (c) and (d) Seasonally-averaged temperature and salinity (determined from 2009–2010 SODA data) at the locations shown by the '+' symbols in (a) and (b).

The computed temperature driven by local heat flux (green line in Fig. 5a) exhibits a seasonal signal similar to observed temperature fields but with the minima and maxima occurring 1–2 months later (Figs. 4a and 5a). In addition, the computed temperature series shows a long-term decline (of roughly 0.8 °C yr^{-1}) that is not matched by the observations (Fig. 5a). This trend in the computed temperature cannot be attributed to the omission of vertical mixing, as mixing with the cooler water below the permanent pycnocline (Fig. 2) would tend to reduce near-surface temperatures even further.

Reflecting the dominance of evaporation over precipitation, the computed salinity series driven only by surface mass flux shows a steady increase with time and no vestige of a seasonal signal (Figs. 4b and 5b). Altering this trend to match the salinity observations requires both a long-term delivery of lower salinity near-surface water to the region as well as a mechanism to produce the observed seasonal oscillations.

3.2.2. The effect of alongshore advection

Evaluating the impact of alongshore advection on the seasonal temperature and salinity signals from Eqs. (8) and (9) required estimates of $V(t)$, dS/dy, and dT/dy. In estimating the latter two properties, we used SODA temperature and salinity data from 2009–2010. These data show that near-surface temperatures (averaged over the upper 50 m) tend to decline going northward over the central and northern Red Sea (Fig. 6a). A similar trend

has been observed based on analysis of SST data (Raitsos et al., 2013) and hydrographic survey measurements (Neumann and McGill, 1962; Maillard and Soliman, 1986; Sofianos and Johns, 2007). Also shown by the SODA data is a tendency for the near-surface salinity to increase going northward over the entire Red Sea (Fig. 6b), consistent with trends observed by hydrographic survey data (Neumann and McGill, 1962; Maillard and Soliman, 1986; Sofianos and Johns, 2007). To estimate dS/dy and dT/dy in our study area, we used temperature and salinity data from SODA grid cells extending between 18 and 22.5°N and arranged in roughly the alongshore direction (Fig. 6a and b). Averages (over the upper 50 m) of near-surface temperature and salinity from these cells show alongshore gradients that do not appear to vary appreciably with season (Fig. 6c and d). Based on these averages, we assigned values to dT/dy and dS/dy of $-0.2/111$ °C km^{-1} and $0.35/111$ psu km^{-1}, respectively (i.e., 0.2 °C decrease and a 0.35 psu increase over a degree of latitude).

In specifying $V(t)$, we assumed that the velocity signal impacting the seasonal temperature and salinity signals varied on a similar time scale as these signals and can be expressed as

$$V(t) = a \sin\left[\frac{2\pi t}{P} + \phi\right] + V_o \tag{10}$$

where a is the sinusoidal flow amplitude, P is the period of 1 year, V_o is the long-term mean flow and ϕ is a phase relative to the beginning of each year. Surface geostrophic velocities determined from the SLA data tend to support this form of a seasonal velocity signal in that they show a tendency for alongshore velocity to be directed northward over winter–spring and southward over summer–autumn (Figs. 4d and 5c). To assign the required parameters in Eq. (10), we used a 6-year (2009–2014) series of alongshore (N–S) geostrophic velocity determined from SLA data in the vicinity of our study area (19–20.5°N; 37.5–38° E). Applying a nonlinear least-squares regression technique (with MATLAB function *nlinfit*) to fit Eq. (10) to this time series gave estimates of $a = 0.047$ (± 0.003, 95% confidence interval) m s^{-1}, $V_o = 0.017$ (± 0.018) m s^{-1} and $\phi = 0.136$ (± 0.057) (zero crossings at June 23 and December 23).

Inclusion of the advection terms in Eqs. (8) and (9) has two principal effects on the computed temperature and salinity series. One is that the mean influx of warmer and less saline water from the south, carried by the steady northward flow, counteracts the long-term trend of declining temperatures and rising salinities seen in the series computed with only the local surface flux terms (Figs. 4 and 5). These trends are not apparent in the series computed with the addition of the advection term. The second effect is produced by the yearly oscillation in alongshore velocity and most profoundly affects the computed salinity signal, which acquires a seasonal variation with the inclusion of the advection term (Fig. 4b and d).

It is unrealistic to expect a close match between the observed and computed temperature and salinity series as our crude calculation omits many factors that may influence near-surface temperature and salinity. These include, but are not limited to, mixing of water across the permanent pycnocline, temporal variations in the alongshore temperature and salinity gradients, differences between the actual flows and our representation of the alongshore velocity signal and the effect of across-shore advection. Nevertheless, the seasonal signals of the temperature and salinity series computed with the inclusion of the advection terms exhibit many of the features of the observed seasonal signals. In close agreement with observed temperatures, the computed temperature series has a seasonal signal spanning a range of roughly 6 °C, with minima close to 26 °C in late-winter/early spring and maxima near 32 °C predominately occurring in late autumn (Figs. 4a and 5a). The seasonal signal of the computed salinity series resembles observed salinity signal in that it extends over a range of roughly 1.2 psu, with maxima winter and minima in early summer (Figs. 4b and 5b). Notably, the observed 3-month phase difference between the observed seasonal temperature and salinity series (with temperature leading) is reproduced by the computed series (Fig. 5).

However, there are differences between the computed and observed seasonal temperature and salinity signals worth noting. The seasonal variation of the computed temperature series is somewhat smaller (by ~ 1 °C) than the range of the observed temperatures (Figs. 4a and 5a). The seasonal signal of the computed salinity series roughly matches that observed at the mooring, but does not show the abrupt decline in salinity observed in February 2015 (Fig. 5b). The long-term salinity signal determined from the SPS survey data is roughly in phase with the computed salinity signal, but varies over a much smaller range (Fig. 5b). We can offer no clear reason as to why the range of the survey-averaged salinities is smaller than the range of the salinities derived from the computations and the mooring data. One possibility is that the survey-derived salinities, which are essentially point measurements, do not capture the full range of the seasonal signal as they are aliased by salinity variations on time scales shorter than that of the seasonal signal.

4. Discussion and conclusions

As noted in Section 3.1.1, our observation is not the first of a dominant seasonal signal in near-surface temperature records from the Red Sea, as this was previously reported by Churchill et al. (2014a). The similarity of the seasonal oscillations of near-surface temperature observed in our study with those detected further to the north and on the eastern side of the Red Sea by Churchill et al. (2014a) suggests that such oscillations may be a ubiquity over the central Red Sea. Our analysis has revealed that these oscillations cannot be solely ascribed to local surface heat exchange, as this would produce a long-term heat loss and a multiyear decline in near-surface temperature. According to the results of our simple heat-flux model, the long-term trend of heat loss through surface exchange near Port Sudan is largely balanced by the advection of warmer water from the south. In our model, this advection is the product of a long-term mean northward flow, inferred from analysis of SLA fields, and a tendency for temperatures to increase going southward from Port Sudan, as deduced from SODA data. Presently, there are no published long-term velocity records to verify the existence of a long-term mean northward flow off of Port Sudan. It is noteworthy, however, that such a flow often appears in the results of hydrodynamic models of the Red Sea, taking the form of a western boundary current flowing northward over the southern and central Red Sea (Sofianos and Johns, 2003; Yao et al., 2014b; Zhai et al., 2015). The alongshore temperature gradient inferred from the SODA data is associated with a near-surface temperature maximum in the central/southern Red Sea south of Port Sudan. As noted in a review by Morcos (1970), this feature of the Red Sea surface temperature field has been recognized since the early twentieth century. More recently, it has appeared in large-scale survey data (Maillard and Soliman, 1986; Sofianos and Johns, 2007), SST fields derived from satellite measurements (Raitsos et al., 2013) and hydrodynamic model results (Sofianos and Johns, 2003). In interpreting their model results, Sofianos and Johns (2003) ascribe the surface temperature maximum to relatively weak winds in the central Red Sea area of wind convergence.

Our observations show that near-surface salinity variations off of Port Sudan are also dominated by a seasonal signal. Because of the dominance of evaporation over precipitation in the Red Sea, the observed oscillations in near-surface salinity cannot be attributed to local mass flux at the surface, as this would produce

a nearly steady increase in near-surface salinity. Our simple salt-flux model indicates that this tendency for salinity to increase due to local evaporation is largely balanced by a northward flux of less saline water from the south. The trend of increasing near-surface salinity going northward over the Red Sea is commonly seen in both observations and model results (Morcos, 1970; Clifford et al., 1997; Sofianos and Johns, 2003, 2007; Yao et al., 2014a, b; Triantafyllou et al., 2014; Churchill et al., 2014b; Dreano et al., 2016). This northward salinity increase has largely been attributed to the influx of relatively low salinity water into the southern Red Sea through the Strait of Bab al-Mandeb. It is well documented that this influx takes two forms. During summer and early autumn, low-salinity water, commonly referred to as Gulf of Aden Intermediate Water, enters the Red Sea in a subsurface (30–120 m) layer (Patzert, 1974; Murray and Johns, 1997; Aiki et al., 2006; Churchill et al., 2014b; Zhai et al., 2015). During the rest of the year, low salinity water, commonly referred to as Gulf of Aden Surface Water, enters the Red Sea over a surface layer of order 50 m depth (Murray and Johns, 1997; Smeed, 2004).

Our analysis indicates that the yearly oscillations in near-surface salinity off of Port Sudan may be largely due to the advection of the alongshore salinity gradient by yearly oscillations of the alongshore velocity. As noted by Sofianos and Johns (2003), seasonal variations in Red Sea flow patterns are likely as in the Red Sea 'both wind and thermohaline forcing are highly variable at the seasonal timescales'. Seasonal averages of their modeled flows in the Port Sudan area are consistent with the alongshore velocity component derived from the SLA data (Fig. 5), directed northward over winter (September–May) and southward over the summer (June–August) (Figs. 4 and 5 of Sofianos and Johns (2003)).

Prominent among the flux terms not included in our analysis are those associated with vertical mixing and across-shore advection. Although we cannot estimate vertical mixing with the data used in our study, we can assert that vertical mixing through the permanent pycnocline would not counteract the long-term trend of declining temperatures and rising salinity associated with local heat and mass exchange through the surface. Because cooler and more saline water is found below the pycnocline, vertical mixing through the pycnocline would tend to further reduce temperature and increase salinity in near surface waters.

Given the prevalence of basin-scale eddies within the central Red Sea (Zhan et al., 2014), it is likely that eddies may frequently cause exchange of near-shore and basin water within the central Red Sea. However, because the eddy lifespan is typically 6 weeks (Zhan et al., 2014), this exchange is likely to produce temperature and salinity changes at intervals relatively short compared with the observed seasonal signals of temperature and salinity.

Although our study has provided new insight into the character and dynamics of seasonal temperature and salinity changes in the Red Sea, it has been based on limited data from a small region and has not specifically dealt with the full suite of dynamics that may influence seasonal temperature and salinity changes. For example, it remains unclear to what extent vertical mixing may influence the observed yearly oscillations of temperature and salinity. It is uncertain to what degree our findings are applicable to other areas of the Red Sea, which may experience different seasonal currents and conditions of heat and mass exchange than in the region near Port Sudan. Perhaps most importantly, further research is required to understand how seasonal variations in temperature and salinity may be influenced by a changing climate, and how this may in turn affect the flora and fauna of the coastal Red Sea.

Acknowledgments

The SPS surveys were funded by the Norwegian Norad's Program for Master Studies and organized by IMR–RSU in Port Sudan. We thank the captain and crew of the Sudanese Marine Security Department ships, which were used for sampling. The PSH surveys were organized and funded by IMR–RSU though the local Environmental Monitoring Program. The mooring and attached instrumentation were funded by the Michelsen Centre for Research-based Innovation in Measurements Science and Technology (MIMT) in Bergen. We are grateful to the captain and crew of the Sudanese Sea Port Corporation tugboat used for deployment. We are thankful to Prof. Abdel Gadir D. El Hag and Prof. Mohamad E.A. Hamza (former directors of IMR) for their support, and also to the IMR staff for making the data collection possible.

NCEP Reanalysis-2 data and NOAA High Resolution SST data were obtained from the NOAA/OAR/ESRL PSD, Boulder, Colorado, USA (http://www.esrl.noaa.gov/psd/). The central Red Sea mooring data were acquired as part of a WHOI–KAUST collaboration funded by Award Nos. USA00001, USA00002, and KSA00011 to the WHOI by the KAUST in the Kingdom of Saudi Arabia. The work of I. Skjelvan and A.M. Omar was partly supported by the Research Council of Norway through the MIMT Center for Research-based Innovation. This work is part of a Ph.D. project at GFI–UiB funded by the Norwegian Quota program.

References

Aiki, H., Takahashi, K., Yamagata, T., 2006. The Red Sea outflow regulated by the Indian monsoon. Cont. Shelf Res. 26, 1448–1468.

Belkin, I.M., 2009. Rapid warming of large marine ecosystems. Prog. Oceanogr. 81, 207–213.

Berman, T., Paldor, N., Brenner, S., 2003. Annual SST cycle in the Eastern Mediterranean, Red Sea and Gulf of Elat. Geophys. Res. Lett. 30, 1261. http://dx.doi.org/10.1029/2002GL015860. 5.

Bower, A.S., Farrar, J.T., 2015. Air–sea interaction and horizontal circulation in the Red Sea. In: Rasul, N.M.A., Stewart, I.C.F. (Eds.), The Red Sea. Springer-Verlag, Berlin, pp. 329–342.

Cantin, N.E., Cohen, A.L., Karnauskas, K.B., Tarrant, A.M., McCorkle, D.C., 2010. Ocean warming slows coral growth in the central Red Sea. Science 329, 322–325.

Carton, J.A., Giese, B., 2008. A reanalysis of ocean climate using simple ocean data assimilation (SODA). Mon. Weather Rev. 136, 2999–3017.

Churchill, J.H., Bower, A.S., McCorkle, D.C., Abualnaja, Y., 2014b. The transport of nutrient-rich Indian Ocean water through the Red Sea and into coastal reef systems. J. Mar. Res. 72, 165–181.

Churchill, J.H., Lentz, S.J., Farrar, J.T., Abualnaja, Y., 2014a. Properties of Red Sea coastal currents. Cont. Shelf Res. 78, 51–61. http://dx.doi.org/10.1016/j.csr.2014.01.025.

Clifford, M., Horton, C., Schmitz, J., Kantha, L.H., 1997. An oceanographic nowcast/forecast system for the Red Sea. J. Geophys. Res. 102, 25,101–25,122.

Davis, K.A., Lentz, S.J., Pineda, J., Farrar, J.T., Starczak, V.R., Churchill, J.H., 2011. Observations of the thermal environment on Red Sea platform reefs: a heat budget analysis. Coral Reefs 30, 25–36.

Dreano, D., Raitsos, D.E., Gittings, J., Krokos, G., Hoteit, I., 2016. The Gulf of Aden intermediate water intrusion regulates the Southern Red Sea summer phytoplankton blooms. PLoS One 11 (12), e0168440. http://dx.doi.org/10.1371/journal.pone.0168440.

Farrar, J.T., Lentz, S., Churchill, J., Bouchard, P., Smith, J., Kemp, J., Lord, J., Allsup, G., Hosom, D., 2009. King Abdullah University of Science and Technology (KAUST) mooring deployment cruise and fieldwork report, technical report. Woods Hole Oceanographic Institute, Woods Hole, Mass, p. 88.

Ferrier-Pages, C., Gattuso, J., Jaubert, J., 1999. Effect of small variations in salinity on the rates of photosynthesis and respiration of the zooxanthellate coral *Stylophora pistillata*. Mar. Ecol. Prog. Ser. 181, 309–314.

Furby, K.A., Bouwmeester, J., Berumen, M.L., 2013. Susceptibility of central Red Sea corals during a major bleaching event. Coral Reefs 32. http://dx.doi.org/10.1007/s00338-012-0998-5.

Guildline, 2002. Portasal Salinometer Datasheet, Model 8410A, Guildline Instrument limited, Ontario, Canada.

Kalnay, E., et al., 1996. The NCEP/NCAR 40-year reanalysis project. Bull. Am. Meteorol. Soc. 77, 437–471.

Kuanui, P., Chavanich, S., Viyakarn, V., Omori, M., Lin, C., 2015. Effects of temperature and salinity on survival rate of cultured corals and photosynthetic efficiency of zooxanthellae in coral tissues. Ocean Sci. J. 50 (2), 263–268.

Large, W.G., Pond, S., 1981. Open ocean momentum flux measurements in moderate to strong winds. J. Phys. Oceangr. 11, 324–336.

Maillard, C., Soliman, G., 1986. Hydrography of the Red Sea and exchanges with the Gulf of Aden in summer. Oceanol. Acta 9 (3), 249–269.

Manasrah, R., Hasanean, H.M., Al-Rousan, S., 2009. Spatial and seasonal variations of sea level in the Red Sea, 1958–2001. Ocean Sci. J. 44, 145–159.

Morcos, S.A., 1970. Physical and chemical oceanography of the Red Sea. Oceanogr. Mar. Biol. Annu. Rev. 8, 73–202.
Morcos, S., Soliman, G.F., 1974. Circulation and deep water formation in the Northern Red Sea in winter (Based on R/V Mabahisss sections, January–February, 1935). In: L'Oceánographie physique de la Mer Rouge. Centre National pour l'Exploration des Oceáns (CNEXO), Paris, pp. 91–103.
Murray, S.P., Johns, W., 1997. Direct observations of seasonal exchange through the Bab el Mandeb Strait. Geophys. Res. Lett. 24, 2557–2560.
Neumann, A.C., McGill, D.A., 1962. Circulation of the Red Sea in early summer. Deep Sea Res. 8, 223–235.
Patzert, W.C., 1974. Wind-induced reversal in Red Sea circulation. Deep Sea Res. 21, 109–121.
Pedgley, D.E., 1974. An outline of the weather and climate of the Red Sea. In: L'Oceánographie Physique de la Mer Rouge. Cent. Natl pour l'Exploration des Oceáns, Paris, pp. 9–27.
Quadfasel, D., Baudner, H., 1993. Gyre-scale circulation cells in the Red Sea. Oceanol. Acta 16, 221–229.
Raitsos, D.E., Hoteit, I., Prihartato, P.K., Chronis, T., Triantafyllou, G., Abualnaja, Y., 2011. Abrupt warming of the Red Sea. Geophys. Res. Lett. 38, L14601. http://dx.doi.org/10.1029/2011GL047984.
Raitsos, D.E., Pradhan, Y., Brewin, R.J.W., Stenchikov, G., Hoteit, I., 2013. Remote sensing the phytoplankton seasonal succession of the Red Sea. PLoS One 8 (6), e64909. http://dx.doi.org/10.1371/journal.pone.0064909.
Raitsos, D.E., Yi, X., Platt, T., Racault, M.-F., Brewin, R.J.W., Pradhan, Y., Papadopoulos, V.P., Sathyendranath, S., Hoteit, I., 2015. Monsoon oscillations regulate fertility of the Red Sea. Geophys. Res. Lett. 42, 855–862. http://dx.doi.org/10.1002/2014GL062882.
Reynolds, R.W., Smith, T.M., Liu, C., Chelton, D.B., Casey, K.S., Schlax, M.G., 2007. Daily high-resolution-blended analyses for sea surface temperature. J. Clim. 20, 5473–5496.
SAIV, 2006. Operating manual for SAIV CTD model 204 with sound velocity and optional sensors. SAIV Company, Bergen, Norway.
Sarmiento, J.L., Gruber, N., 2006. Ocean Biogeochemical Dynamics. Princeton University Press, Princeton, NJ, USA.
Smeed, D.A., 2004. Exchange through the Bab el Mandab. Deep Sea Res. Part I 51, 455–474.
Sofianos, S.S., Johns, W.E., 2001. Wind induced sea level variability in the Red Sea. Geophys. Res. Lett. 28, 3175–3178.
Sofianos, S.S., Johns, W.E., 2003. An oceanic general circulation model (OGCM) investigation of the Red Sea circulation: 2. Three-dimensional circulation in the Red Sea. J. Geophys. Res. 108 (C3), 3066. http://dx.doi.org/10.1029/2001JC001185.
Sofianos, S.S., Johns, W.E., 2007. Observations of the summer Red Sea circulation. J. Geophys. Res. 112, C06025. http://dx.doi.org/10.1029/2006JC003886.
Sultan, S.A.R., Ahmad, F., 1991. Long-term temperature and salinity variations near Jeddah in relation to certain meteorological factors over the Red Sea. J.K.A.U.: Mar. Sci. 2, 19–29.
Sumner, D., Belaineh, G., 2005. Evaporation, precipitation, and associated salinity changes at a humid, subtropical estuary. Estuaries 28 (6), 844–855.
Triantafyllou, G., Yao, F., Petihakis, G., Tsiaras, K.P., Raitsos, D.E., Hoteit, I., 2014. Exploring the Red Sea seasonal ecosystem functioning using a three-dimensional biophysical model. J. Geophys. Res.: Oceans 119, 1791–1811. http://dx.doi.org/10.1002/2013JC009641.
Wafar, M., Qurban, M.A., Ashraf, M., Manikandan, K.P., Flandez, A.V., Balala, A.C., 2016. Patterns of distribution of inorganic nutrients in Red Sea and their implications to primary production. J. Mar. Syst. 156, 86–98.
Wallcraft, A.J., Kara, A.B., Hurlburt, H.E., Chassignet, E.P., Halliwell, G.H., 2008. Value of bulk heat flux parametrizations for ocean SST prediction. J. Mar. Syst. 74, 241–258.
Yao, F., Hoteit, I., Pratt, L.J., Bower, A.S., Kohl, A., Gopalakrishnan, G., Rivas, D., 2014a. Seasonal overturning circulation in the Red Sea: 2. Winter circulation. J. Geophys. Res.: Oceans 119, 2263–2289. http://dx.doi.org/10.1002/2013JC009331.
Yao, F.C., Hoteit, I., Pratt, L.J., Bower, A.S., Zhai, P., Kohl, A., Gopalakrishnan, G., 2014b. Seasonal overturning circulation in the Red Sea: 1. Model validation and summer circulation. J Geophys. Res.-Ocean 119, 2238–2262.
Zhai, P., Bower, A.S., Smethie, W.M., Pratt, L.J., 2015. Formation and spreading of Red Sea Outflow Water in the Red Sea. J. Geophys. Res.: Oceans 120 (9), 6542–6563. http://dx.doi.org/10.1002/2015JC01075.
Zhan, P., Subramanian, A.C., Yao, F., Hoteit, I., 2014. Eddies in the Red Sea: A statistical and dynamical study. J. Geophys. Res.: Oceans 119, 3909–3925. http://dx.doi.org/10.1002/2013JC009563.